

Numerical Heat Transfer, Part A: Applications

An International Journal of Computation and Methodology

ISSN: 1040-7782 (Print) 1521-0634 (Online) Journal homepage: <http://www.tandfonline.com/loi/unht20>

Modeling of compressible phase-change heat transfer in a Taylor-Bubble with application to pulsating heat pipe (PHP)

Nikhilesh Ghanta & Arvind Pattamatta

To cite this article: Nikhilesh Ghanta & Arvind Pattamatta (2016) Modeling of compressible phase-change heat transfer in a Taylor-Bubble with application to pulsating heat pipe (PHP), Numerical Heat Transfer, Part A: Applications, 69:12, 1355-1375, DOI: [10.1080/10407782.2016.1139980](https://doi.org/10.1080/10407782.2016.1139980)

To link to this article: <http://dx.doi.org/10.1080/10407782.2016.1139980>



Published online: 13 May 2016.



Submit your article to this journal [↗](#)



Article views: 2



View related articles [↗](#)



View Crossmark data [↗](#)

Modeling of compressible phase-change heat transfer in a Taylor-Bubble with application to pulsating heat pipe (PHP)

Nikhilesh Ghanta and Arvind Pattamatta

Heat Transfer and Thermal Power Lab, Indian Institute of Technology Madras, Chennai, Tamil Nadu, India

ABSTRACT

The present work deals with the development of a compressible phase-change solver and implementation toward the numerical modeling and investigation of a part-unit cell of a pulsating heat pipe (PHP). The fundamental understanding of the working of the part-unit cell is imperative in the development of a complete Computational Fluid Dynamics (CFD) model of a PHP. The compressible model developed in the present work is based on the Volume-of-Fluid solver of the open source CFD software, OpenFOAM, in which the contour-based interface reconstruction algorithm and the contact-line evaporation model have been incorporated. Owing to the lack of a single standard benchmark validation case for a compressible phase-change solver, a huge emphasis in the present work is laid on the solver development and validation, the latter part of which is conducted in stages. Furthermore, simulations for the formation of a Taylor-Bubble through a constrained bubble growth are performed and the fallacy of an incompressible solver is shown distinctly. The validated solver is used to model a part-unit cell of a PHP and a parametric study is performed on the part-unit cell. The effect of variation of evaporator length, evaporator superheat, and liquid fill ratio on the performance of the PHP is discussed.

ARTICLE HISTORY


Received 4 September 2015

Accepted 2 December 2015

1. Introduction

Pulsating heat pipe (PHP) is a very good heat transfer device of great utility in modern electronic components, wherein the heat release flux per unit area is ever increasing. One of the early experimental studies on oscillatory slug flows involved in PHP was carried out by Khandekar et al. [1]. They also worked on the impact of the filling ratio on the effect of the bubbles in the two-phase oscillating flow. At higher filling ratios (95% of liquid), the Taylor-Bubbles hindered the two-phase fluid motion. One of the most recent efforts in understanding the oscillatory flow phenomenon and the heat transfer characteristics in the oscillating flow of Taylor-Bubbles is made by Rao et al. [2]. This work was more concentrated on explaining the oscillating phenomenon of the liquid-vapor interface. The meniscus oscillations were studied experimentally and explained analytically to some extent. The effect of the compressibility of the vapor phase involved is emphasized by the results of Rao et al. [2].

Numerous theoretical models have been developed to understand the hydrodynamic and heat transfer processes involved in the slug flow of a PHP. The two-phase heat transfer phenomenon is of prime importance to the model and this modeling has come about in various stages. In the primary stages, Zuo et al. [3] started off with a simple spring-mass-damper. The heat transfer phenomenon was just accounted in the model by affecting the parameters of the system, hence keeping the basic

CONTACT Arvind Pattamatta  arvindp@iitm.ac.in  Heat Transfer and Thermal Power Lab, Indian Institute of Technology Madras, Chennai 600036, Tamil Nadu, India.

Color versions of one or more of the figures in the article can be found online at www.tandfonline.com/unht.

© 2016 Taylor & Francis

Nomenclature

a	major-axis length of ellipse, m	Δx	length interval, m
b	minor-axis length of ellipse, m	ρ	density, kg/m ³
c	specific heat capacity, J/(kg K)	$\dot{\rho}_0$	sharp mass source term field, kg/(m ³ s)
D	diameter, m	$\dot{\rho}_1$	smearred mass source term field, kg/(m ³ s)
F	volume fraction of the liquid phase, -	γ	polytropic constant, -
F_s	surface tension force, N	μ	dynamic viscosity, Pa s
f1	objective function 1, -	σ	surface tension, N/m
g	acceleration due to gravity, m/s ²	κ	interface curvature, 1/m
\dot{j}	phase-change mass flux, kg/(m ² s)	ϕ	any arbitrary vector field, -
k	thermal conductivity, W/(m K)		
L	length, m	Subscripts	
p	pressure, Pa	A	adiabatic section
R	heat resistance, K m ² /W	E	evaporator
	radius, m	F	liquid fill region
s	second, s	I	component/phase
T	temperature, K	L	liquid
t	time, s	V	vapor
U	velocity vector, m/s	Int	interface
u	magnitude of velocity, m/s	Lv	difference of the parameter between liquid and vapor phases
V	volume, m ³	Max	maximum
Δh	change in enthalpy, J/kg	Sat	saturation
Δt	time step, s	∞	infinity
$\Delta \tau$	artificial time step, s		

model as a simplified hydrodynamic model. However, the main drawback of this model is its inability to predict the heat transfer performance. The numerical model of approximating the oscillatory Taylor-Bubble (T-B) flow to a spring-mass-damper system was made better by including multiple spring-mass-dampers by Wong et al. [4]. However, the thermodynamic characteristics were still to be modeled and the phase-change process accounted for. One of the major attempts at developing a theoretical model to accurately simulate the behavior of liquid slugs and vapor slugs was made by Shafii et al. [5]. They included the heat transfer mechanism in the model. The oscillating or pulsating motion of the liquid slugs (Taylor-Bubbles) was studied in greater detail by Ma et al. [6]. Their model considers the thermal energy from the temperature difference between the evaporator and the condenser as the driving force for the oscillatory motion, which will overcome the frictional force and the force due to the deformation of compressible bubbles. A more sophisticated thermal analysis of the two-phase oscillatory flow was presented in the work of Zhang and Faghri [7].

To date, there are no Computational Fluid Dynamics (CFD)-based numerical models to accurately simulate the complex thermo-hydrodynamics of a PHP. Development of one such complete numerical model alongside performing experimental work will result in a better understanding of the working of a PHP. One of the primary numerical models explaining the heat transfer phenomenon in two-phase flows in a microchannel was developed by Mukherjee and Kandlikar [8]. They analyzed the growth of a vapor bubble during flow of water in a microchannel. A numerical study on the contribution of thin-film evaporation during flow boiling in microchannels was carried out by Mukherjee [9]. This is an extension of the work performed by Thome et al. [10] and involved a better developed numerical model. Further developing the heat transfer models, Liu and Hao [11] worked on one of the first CFD-based comprehensive mathematical models involving the vapor-liquid interface and surface tension in an oscillatory two-phase flow. It was a successful attempt at describing the vapor-liquid two-phase flow, heat, and mass transfers and phase-change processes in the two-phase T-B flows. The slug flow was predicted using the model developed and the results were in good agreement with the experimental observations qualitatively. In this model, to maintain the quality and energy conservation in the process of phase change, the Volume of Flow (VOF) method is used to describe the positions and motions of the vapor-liquid interfaces. Pattamatta et al. [12] worked on

the numerical investigation of the phase-change characteristics of a Taylor-Bubble during flow boiling in a minichannel. They developed a numerical model and implemented it in OpenFOAM. A detailed parametric study was performed on the Taylor-Bubble nucleation characteristics.

However, none of the numerical models considered thus far accounted for the compressibility of the vapor phase, which is important in capturing the expansion and compression process undergone by a Taylor-Bubble in a PHP. In addition, there were no numerical studies on the fundamental working of a unit cell of a PHP. The present work attempts to bridge the gap and explain the importance of compressibility effects in the working of a unit cell of a PHP. In this study, a compressible solver is developed in OpenFOAM based on the Volume-of-Fluid model.

2. Numerical methodology and formulation

The basic equations involved in the simulations using the finite volume method are the continuity equations and the conservation equations for momentum and energy. The compressible version of these equations used in developing the numerical model is as follows:

$$\frac{\partial \rho}{\partial t} + \nabla \cdot (\rho U) = \dot{\rho}_0 \quad (1)$$

$$\frac{\partial (\rho U)}{\partial t} + \nabla \cdot (U \cdot \rho U) - \rho g = -\nabla p + \nabla \cdot \left[\mu \left(\nabla U + (\nabla U)^T \right) \right] - F_s \quad (2)$$

$$\frac{\partial \rho c T}{\partial t} + \nabla \cdot (\rho c U T) - \nabla \cdot (k \nabla T) - P \nabla \cdot V = \dot{\rho}_0 \Delta h_v + \dot{\rho}_0 c T \quad (3)$$

where F_s is the surface tension force at the interface, given by $F_s = \frac{2\rho\delta_s}{(\rho_0+\rho_1)}[\sigma\kappa n]$, ρ is the density, U is the velocity vector, p is the pressure, μ is the dynamic viscosity, c is the specific heat capacity, T is the temperature, k is the thermal conductivity, σ is the surface tension, and κ is the interface curvature. $\dot{\rho}_0$ is the volumetric source term, introduced to incorporate the mass flux (calculated from the phase-change model) into the conservation equations.

$$\dot{\rho}_0 = j_{int} \frac{|\vec{S}_{int}|}{V_{cell}} \quad (4)$$

The value that results from the source term defined in Eq. (4) can be very large near the interface. It will also be zero elsewhere. Hence, it is not directly used in the conservation equations, but modified by the approach of Hardt and Wondra [13]. This approach involves changing the sharp definition of source terms as described above into a relatively smooth distribution. The smearing of the sharp source term of the above-mentioned equation is as follows:

$$\dot{\rho}_1 - \nabla \cdot [(D\Delta\tau)\nabla\dot{\rho}_1] = \dot{\rho}_0 \quad (5)$$

where $\Delta\tau$ is the artificial time step.

For the continuity equation, the source field term, represented by $\dot{\rho}_0$, accounts for the nonzero velocity field divergence, where mass is either added or removed. The source field term in the energy equation has two contributions, first the contribution of energy due to phase change at the interface, and second, to account for the velocity field, which turns out to have a nonzero divergent value, resulting from the added or removed mass in the pure vapor or liquid cells. The part of the source term containing the first contribution mentioned above is calculated using the sharp source term and the enthalpy of vaporization. The second term compensating for the erratic velocity field is calculated using the smooth source term. This is needed to compensate for the additional sensible heat addition or removal due to the source terms. The final energy equation also involves the additional pressure work term, resulting from the added feature of the compressibility of the medium.

The numerical procedure used to solve the Navier Stokes equation is the PIMPLE algorithm. It is a merged PISO (Pressure-Implicit with Splitting of Operator) and SIMPLE (Semi-Implicit Method for Pressure Linked Equations) algorithm.

Of the various methods available to simulate two-phase flows, the one used in the present study is the Volume-of-Fluid (VOF) method. It was first developed by Hirt and Nickolas [14]. The VOF method captures a moving interface on a numerical mesh. The primary concept in a VOF method is the use of Volume Fraction F_i , which is the partial volume of the phase i in the control volume. The volume fraction field is transported only by the velocity field and is used as shown in Eq. (6).

$$\frac{\partial F}{\partial t} + \nabla \cdot (UF) + \nabla \cdot \{c_F |\bar{u}| \bar{n} [F(1-F)]F\} = \frac{\dot{\rho}}{\rho} F \quad (6)$$

The third term on the left-hand side of Eq. (6) is a special compression term added by OpenFOAM to ensure the sharpness of the interface. The above equation is solved explicitly with flux-limiting conditions to keep the volume fraction field bounded. As explained above, the resulting velocity field is not free of divergence in cells containing the source terms. Hence, an additional source term has been added to the transport equation for the volume fraction as well, represented by $\frac{\dot{\rho}}{\rho} F$. The surface tension value, which results out of the curvature, is calculated from the Continuum Surface Force (CSF) approach, developed by Brackbill et al. [15]. The sharp local interface reconstruction model used in the present work is taken from Kunkelmann [16].

Assumptions are made to solve the above-mentioned conservation equations. The material properties involved in this study are all taken at saturation conditions, corresponding to the particular pressure at which the simulations are performed. Hence, the material properties are considered to be independent of temperature and pressure. The liquid medium is assumed as incompressible and the fluid to be Newtonian. The equations presented above are incorporated in the OpenFOAM solver and implemented within.

The phase-change model incorporated in the present solver involves the use of local temperature field values to calculate the phase-change mass flux. This results in the knowledge of phase-change mass flux values in each of the cells containing a part of the interface. The local phase-change mass flux is calculated as shown in Eq. (7). This was first implemented by Hardt and Wondra [13]. In their method, the evaporating mass flux is calculated from the interface temperature and the interface heat resistance.

$$j_{int} = \frac{T_{int} - T_{sat}}{R_{int}} \quad (7)$$

The specific region of contact of the liquid-vapor interface and the solid wall is of significance, as this is a three-phase contact region. An apparent contact angle is defined as the angle made by the tangents to the liquid-vapor and the solid-vapor interfaces, as depicted in Figure 1. This can be calculated from the Young equation. Because of the large complexity involved with small length scales, there is no completely physical model available for predicting the dynamics of the contact angle. Hence, simulations performed in the present study take a constant apparent contact angle.

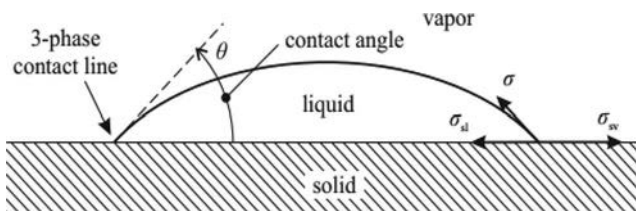


Figure 1. Definition of contact angle; Kunkelmann [16].

The present work incorporates the contact-line model developed by Stephan and Busse [17] and implemented by Kunkelmann [16]. According to this model, the three-phase contact line has three distinct characteristics.

- i. Significance of intermolecular forces of attraction between the fluid and the wall molecules.
- ii. Local thermodynamic equilibrium change caused due to the effect of the curvature and attraction forces.
- iii. Additional temperature drop across the interface during phase change, as a result of a finite heat resistance offered by the interface.

A time step size limitation for the temporal discretization of the computational domain is set by the Courant number. The Courant number should not exceed unity in any case. For the phase-change problems under consideration, a maximum courant number of 0.25 is deemed good.

$$Co = \frac{u\Delta t}{\Delta x} \quad (8)$$

3. Compressible phase-change solver validation

Currently, there are no standard benchmark solutions for validating a compressible phase-change model. This is primarily due to the high complexity of the phase-change phenomenon, which limits the use of analytical approaches. Hence, the solver validation discussed in this work is carried out in stages. In this section, the various stages of solver validation that were performed with the compressible solver are presented and their results discussed. First, the adiabatic compressibility model is validated for the case of unconstrained bubble expansion and contraction using an approximate analytical solution of the Rayleigh–Plesset (RP) equation. For this part of the validation, the phase-change component of the solver is turned off. Later, the phase-change component is validated for an unconstrained bubble growth and contraction scenario due to phase change, using an analytical solution discussed by Carey [18]. Furthermore, a test case with constrained phase change leading to the development of a Taylor-Bubble is considered. However, no analytical solution exists for this case. The same is also simulated with an incompressible version of the solver and comparisons drawn to establish the limitations of using an incompressible solver. The working fluid used for the simulation cases of solver validation is water.

3.1. Bubble characteristics during adiabatic unconstrained bubble expansion and contraction

In this study, a spherical bubble of a given initial radius R_0 , present in an infinite liquid domain of temperature T_∞ and pressure P_∞ , is considered. As the thermal effects are not considered for this part of solver validation, the liquid temperature T_∞ is taken to be a constant. On the other hand, the liquid pressure is considered as a known parameter, which in turn regulates the amount of growth or collapse of the bubble. The liquid density is also assumed to be constant. It is also assumed that the contents of the bubble are homogeneous and that the temperature $T_b(t)$ and pressure $P_b(t)$ within the bubble are always uniform. Owing to the differential pressure across the bubble surface, the bubble either grows or collapses. This dynamic change in the radius of the bubble is calculated analytically from the modified RP equation. Its general form for a polytropic gas is shown in Eq. (9). The effects of fluid viscosity and surface tension are included in the equation, which modify the boundary conditions:

$$R\ddot{R} + \frac{3}{2}\dot{R}^2 = \frac{1}{\rho} \left(\left(p_0 + \frac{2\sigma}{R_0} \right) \left(\frac{R_0}{R} \right)^{3\gamma} - p_0 - P_b(t) - \frac{4\mu}{R}\dot{R} - \frac{2\sigma}{R} \right) \quad (9)$$

Given an initial bubble pressure p_0 , the above equation can be solved to determine $R(t)$, provided $P_b(t)$ is known. $P_b(t)$ can be written in terms of initial bubble pressure p_0 , initial bubble radius R , and $R(t)$. The equation can then be simply solved with a few approximations as will be illustrated now. For any applied pressure of sufficiently low amplitude, the bubble radius $R(t)$ can be approximated as

$$R(t) = R(1 + x(t)), \text{ where } |x| \ll 1$$

Substituting the above approximation in the RP equation, we obtain a second-order term in x , which is neglected owing to the fact that $|x| \ll 1$.

Another approximation is used in the form of binomial expansion, as follows:

$$p_0 \left(\frac{1}{1+x} \right)^{3\gamma} \sim p_0 (1 - 3\gamma x) \quad (10)$$

Substituting the above binomial approximation in the RP equation, the following equation is obtained:

$$\ddot{x} + \frac{4\mu}{\rho R_0^2} \dot{x} + \omega_0^2 x = \frac{-P(t)}{\rho R_0^2} \quad (11)$$

$$\text{where } \omega_0 = \frac{1}{\rho R_0^2} \left[3\gamma \left(p_0 + \frac{2\sigma}{R} \right) - \frac{2\sigma}{R} \right]$$

This is the general solution of a damped linear oscillator. The above equation can be easily solved for various values of p_0 and known hydrodynamic properties of the liquid and gas used.

A test case is set up in OpenFOAM with an initial bubble diameter of 1.5 mm, having an initial pressure of 1.5 bar, and maintained at 300 K. It is placed in a vast domain ($L_{\text{domain}} \gg R_{\text{bubble}}$) of liquid (water) initially having a pressure of 1 bar and maintained at 300 K. The setup of the problem is shown in Figure 2. The simulations are performed on a 2D axisymmetric mesh with a size of $0.1 \text{ mm} \times 0.1 \text{ mm}$.

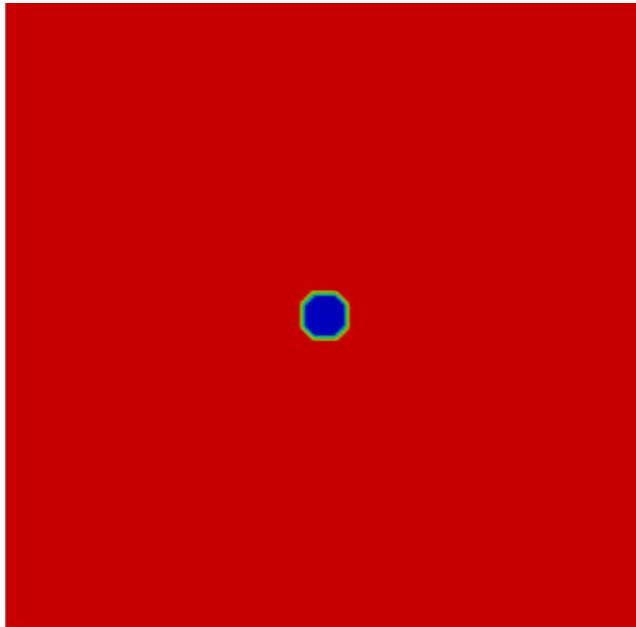


Figure 2. Initial setup of the bubble growth problem in OpenFOAM – a volume fraction contour.

Simulations are run to track the radius of the bubble dynamically as the bubble oscillates to finally settle down at an equilibrium size, which is effectively governed by the Young–Laplace equation. The Young–Laplace equation is a derivative equation of the RP equation, under the conditions of equilibrium. With the values of pressure and initial bubble radius mentioned above, the approximate solution to the RP equation is calculated and plotted as a function of time. Figure 3a gives the comparison of bubble radius normalized with the initial bubble radius, of the simulated case to that of the analytically calculated one from the RP equation, represented by Eq. (9). A good agreement is found between the compressible solver simulated results and the calculated values of the bubble radius. However, the incompressible solver fails to recognize the inertial effects on the volume change of the bubble. The bubble remains the same throughout.

The same is done for the case of bubble shrinkage, where the initial bubble pressure is assumed as 0.8 bar. The net difference in bubble radius is less than that observed in expansion of bubble with 0.5 bar pressure difference, as expected (owing to the lower pressure difference value compared to

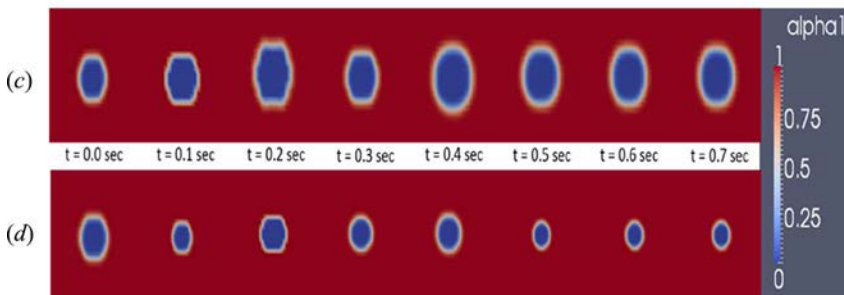
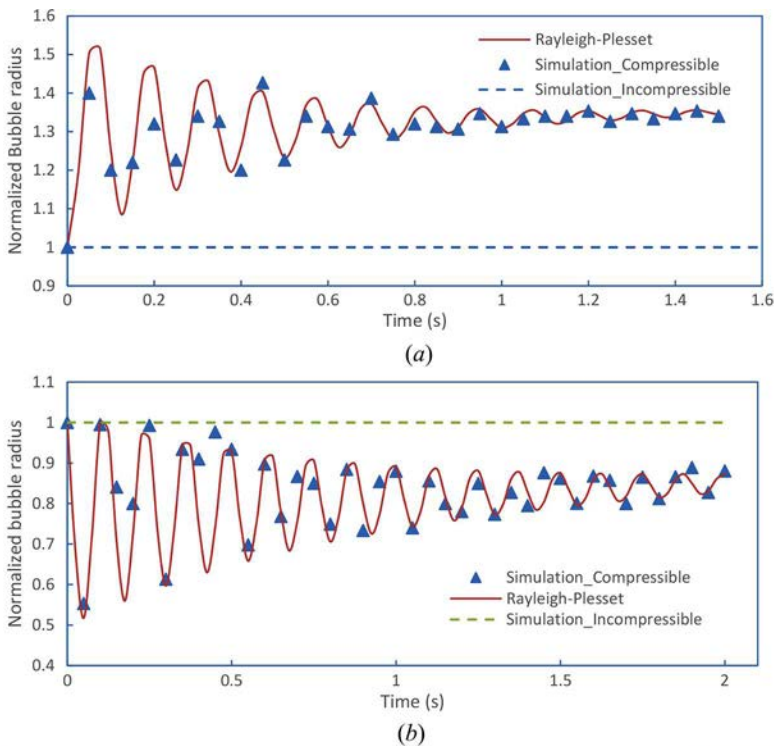


Figure 3. Bubble contraction in case of an adiabatic non-phase change growth, with (a) a bubble excess pressure of 0.5 bar and (b) a surrounding liquid excess pressure of 0.2 bar; time snapshots of volume fraction contours for (c) bubble expansion and (d) bubble contraction.

the previous case). **Figure 3b** shows the normalized bubble radius variation with time, for the cases of simulation and analytical calculation.

Figures 3c, d show the time variant snapshots of volume fraction contours for both bubble expansion and contraction. It is observed that the simulated bubble radius values tracked by the compressible solver at various points of time lie on the curve of solution of the RP equation. The agreement is found to be good. However, the incompressible solver fails to capture this bubble dynamics. This validates the compressible nature of the solver developed, in the absence of the phase-change phenomenon.

3.2. Bubble characteristics during the unconstrained isothermal phase change

The second test case considered for the compressible solver validation is the growth of a spherical bubble of vapor in an infinitely extended liquid, which is either superheated or subcooled, depending on the problem being bubble expansion or contraction, respectively. The spherical symmetry for this case makes it possible to predict the bubble growth phenomenon using simple analytical tools. The different stages of growth have been well described by Plesset and Zwick [19]. At any instant, the rate of bubble growth is dictated by the following three factors:

1. The fluid momentum and pressure difference interactions: Inertial Effects
2. The rate of heat transfer to the interface: Thermal Effects
3. The thermodynamic constraint

When the bubble first forms, the temperature at the interface of the bubble will be nearly equal to the temperature of the superheated liquid. The vapor generated at the interface will also be at a pressure close to $P_{\text{sat}}(T_{\infty})$. In the process of bubble growth, the liquid superheat near the interface is consumed so as to provide the latent heat of vaporization. Simultaneously, the capillary pressure difference across the interface decreases as the radius increases and the pressure inside drops toward P_{∞} . Hence, during the bubble growth process, P_v and T_v will lie in the following ranges:

$$P_{\infty} \leq P_v \leq P_{\text{sat}}(T_{\infty}) \rightarrow \text{Inertia-controlled growth}$$

$$T_{\text{sat}}(P_{\infty}) \leq T_v \leq T_{\infty} \rightarrow \text{Heat transfer-controlled growth}$$

These are two limiting cases of the bubble growth phenomenon, as explained in detail by Carey [18].

In the inertia-controlled growth regime, the growth rate is governed by the momentum interaction between the bubble and the surrounding liquid, as the heat transfer to the interface is very fast and thereby not a limiting factor. This stage dominates during the initial stages of bubble growth, just after the bubble forms and begins to grow. For this case of inertia-dominant bubble growth, the Rayleigh equation is used to derive a relation between bubble radius and time, as shown in Eq. (12):

$$R(t) = \left\{ \frac{2}{3} \left(\frac{[T_{\infty} - T_{\text{sat}}(P_{\infty})]}{T_{\text{sat}}(P_{\infty})} \right) \frac{h_{lv} \rho_v}{\rho_l} \right\}^{1/2} t \quad (12)$$

The above result implies that the bubble radius varies linearly with time during the phase of inertia-controlled growth. This is an approximate solution, as the Rayleigh equation does not take into consideration the effects of viscosity and capillary pressure difference across the interface.

The heat transfer-controlled growth regime is dominant at the later stages of bubble growth, when the bubble size increases and a depletion of liquid superheat near the interface takes place. Here, the bubble growth is limited by a slower transport of heat to the surface. In this case, it can be assumed that the bulk vapor and the liquid-vapor interface are at saturation temperature. As a result, the interface motion is slower compared to that during inertia-controlled growth. Plesset and Zwick [19]

provided an approximate solution for this regime and came up with the following relation for the bubble radius:

$$R(t) = 2C_R \sqrt{(\alpha_l t)}$$

This shows that for the domain controlled by heat transfer, the bubble radius grows proportional to the square root of time.

The above-mentioned two domains comprise only the initial and final phases of the bubble growth. During the intermediate phase, wherein both the inertial effects and thermal effects are equally dominant, there is no analysis for the bubble radius dependence on time. In accordance with the theory discussed above, a case is set up in OpenFOAM where a bubble of initial radius 1.5 mm is placed in an infinite liquid domain. The bubble is initially maintained at a pressure of 1.2 bar compared to the liquid pressure of 1 bar. The bubble is also given a 15° superheat with respect to the surrounding liquid. Simulations are performed on a 2D, axisymmetric mesh with a size of 0.1 mm × 0.1 mm. The bubble radius is tracked with time. The same case was also run, taking the gas involved (water vapor) as incompressible. Figure 4a shows the bubble growth phenomenon, as plotted against

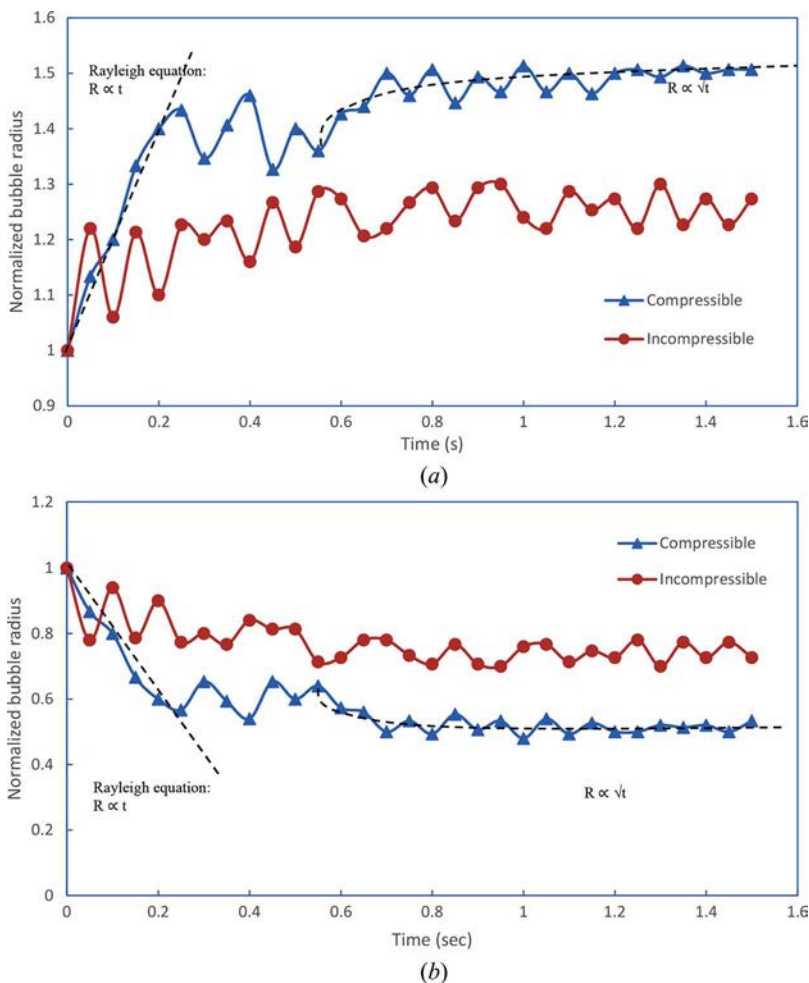


Figure 4. A plot of the normalized bubble radius against time, with (a) an initial bubble excess pressure of 0.2 bar and liquid superheat of 15°C (compressible vs. incompressible solver) and (b) an initial liquid excess pressure of 0.2 bar and vapor superheat of 15°C (compressible vs. incompressible solver).

time. Radius plotted in Figure 4a is normalized with respect to the initial bubble radius. The same plot also shows the difference in the compressible and incompressible solvers for the same test case. The correct trends for both the domains discussed above are also plotted over the graph (dashed line), showing the agreement with the simulated results.

As discussed in theory, the initial stage of bubble growth is found to be short in time, and during that phase, the bubble radius is found to be linearly varying with time. This corresponds to the inertia-controlled bubble growth. Again in the later stages of bubble growth, there is a clear square root dominance of time on bubble radius. This is the heat-transfer-controlled growth. This phase is longer in duration compared with the inertia-controlled one. There is a small zone between the two above-mentioned phases where the relation between bubble radius and time is not very clear. This is the zone where both the inertial and thermal effects come into play with equal importance. This is very complicated to model analytically and hence there are no simple analytical solutions in the literature. From the results shown in Figure 4a, a good agreement is found with the results of the OpenFOAM simulations with the compressible phase-change solver to the theory discussed. Next, the opposite case of bubble contraction with a subcooled liquid is set up. The bubble pressure is reduced to 0.8 bar to allow a 0.2 bar excess pressure in the surrounding liquid. Figure 4b shows the bubble growth characteristics as observed from the simulations, for both a compressible solver and an incompressible solver. As in the case of bubble expansion, the two specific bubble growth regions are visible clearly in the case of bubble contraction.

It is evident from both the bubble expansion and contraction simulation results that the compressible phase-change solver accurately predicts the bubble growth phenomenon as discussed in theory. In contrast, the incompressible solver cannot predict the inertial effects on bubble growth. It is observed in both the bubble expansion and contraction graphs that the bubble radius growth seen in the simulation results of the incompressible solver follows an approximate square root dependence on time, which indicates the influence of heat-transfer effects alone. The incompetency of the incompressible solver to work well in the presence of inertial effects is clearly seen with this case of validation. The main outcome of this second test case is the confirmation that the phase-change model predicts the bubble growth characteristics correctly, considering the gas phase as a compressible medium.

3.3. Taylor-Bubble characteristics during the constrained isothermal phase change

Taylor-Bubble flow is an important regime in the working of a PHP and hence knowledge on the formation characteristics of a Taylor-Bubble is vital for a good understanding of the phenomenon involved in PHP working. Therefore, the final part of the solver testing process involves simulation of the formation and development of a Taylor-Bubble from a simple minute spherical bubble in a capillary tube. This is achieved by constraining the growth of the bubble, expanding under pressure difference between the bubble and the surrounding liquid as well as due to liquid superheat. The OpenFOAM case is set up with an initial bubble diameter of 0.1 mm diameter in a capillary tube of diameter 1 mm. Water is taken as the filling medium around the bubble in the capillary tube. At the start of the simulation, it is ensured that the bubble has an excess pressure of 0.8 bar with respect to the surrounding liquid. In addition to this pressure difference, a liquid superheat of 15° is maintained. Simulation is run on a 2-D, axisymmetric mesh with a mesh size of 0.01 mm × 0.02 mm. Similar to the cases of the previous validation, this case is run with both compressible and incompressible solvers.

Figures 5a, b show the progression of bubble development in both cases of compressible and incompressible solvers. As can be anticipated from the theory discussed in the previous subsection, the starting phase of bubble growth is dominated by the pressure and inertial effects, leading to a sudden jump in the bubble radius. From then on, the growth in the bubble radius is steady, until the bubble surface just reaches the walls of the capillary tube. As established in the previous validation cases, the incompressible solver fails to predict the inertial effects on the growth of the bubble. This

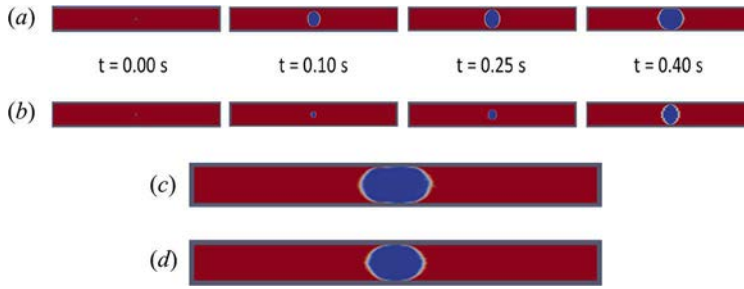


Figure 5. Time snapshots of volume fraction contours during the formation of a Taylor-Bubble, for (a) compressible solver and (b) incompressible solver; volume fraction contours showing the Taylor-Bubble formed after a time of 0.25 s from the loss of the sphericity of the bubble, for (c) compressible solver and (d) incompressible solver.

is again evident in this validation, as seen in Figure 5. The incompressible solver predicts a very slow growth rate of bubble and hence takes a longer time for the spherical bubble to reach the periphery of the capillary tube.

Once the bubble attains the maximum spherical shape it can, i.e., when the bubble fills up the whole cross-sectional area of the capillary tube under consideration, it can no longer grow in the radial direction. Hence, the bubble has only the longitudinal direction to grow, leading to the formation of a Taylor-Bubble. Figure 5c, d shows the stage of the Taylor-Bubble formed. A comparison between the compressible and incompressible solvers is also made.

The growth of the bubble radius is plotted in Figure 6a. The bubble radius is assumed as the equivalent radius corresponding to the instantaneous volume of the bubble. A comparison is made of the bubble growth with the compressible solver to the incompressible one. It is observed that the bubble reaches a higher radius when simulated with a compressible solver to that when done by an incompressible one. The rate of bubble growth is also smaller in case of the incompressible solver.

Once the bubble surface comes in contact with the capillary wall surface, bubble growth occurs only in the longitudinal direction. This is analyzed well considering the aspect ratio of the Taylor-Bubble formed. Aspect ratio is defined as the ratio of the semi-major axis to the semi-minor axis. The aspect ratio definition is depicted in Figure 6c, wherein a sample volume fraction result of a simulation is also shown (Figure 6b).

With this aspect ratio of the Taylor-Bubble in consideration, the development of the bubble is plotted in Figure 6d. It shows the Taylor-Bubble development for both a compressible and an incompressible solver, from the moment the bubble surface comes in contact with the capillary tube surface. It should be noted however that the incompressible solver predicts a larger time for the bubble to completely grow spherically compared to the compressible solver. The zero time in Figure 6d corresponds to the time instant when the bubble has reached the periphery of the capillary tube. As seen in Figure 6d, the compressible solver predicts a larger bubble in a smaller time frame. In the case of the compressible solver, the bubble expanded from an aspect ratio of 1 to 1.92857 in 0.25 sec . The incompressible solver, however, could only reach an aspect ratio of 1.57142 in 0.25 sec from the start of the loss of sphericity of the bubble.

This test case confirms the correctness of the compressible solver incorporated with phase change when applied to a constrained bubble growth, effectively leading to the formation and development of a Taylor-Bubble. Through the various stages of validation described in this section, the developed in-house compressible phase-change solver is ascertained to be validated.

4. Modeling of a part-unit cell of a PHP

4.1. Validation

With the aim to expand this work to a full-scale PHP unit cell in the future, a part-unit cell of a PHP, consisting of the evaporator and the adiabatic sections, was modeled. As the full PHP unit cell is

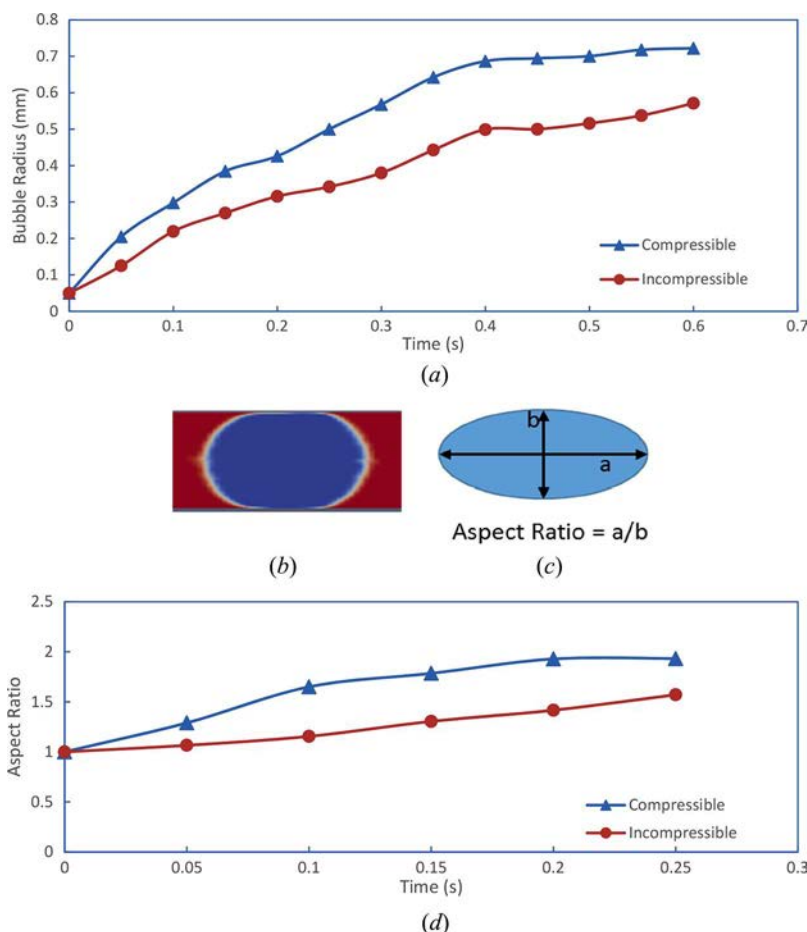


Figure 6. (a) Equivalent bubble radius plotted against time for compressible solver and incompressible solver; (b) a sample Taylor-Bubble simulated by the compressible solver; (c) definition of aspect ratio, as shown by a schematic; (d) variation of the aspect ratio of the Taylor-Bubble: a comparison between compressible and incompressible solvers.

complicated in its working, involving simultaneously phase change (both evaporation and condensation) and inertial effects, it becomes imperative to perform numerical simulations on a part-unit cell in order to obtain a better insight into the physics of the phenomenon taking place. A schematic of the geometry is shown in Figure 7, indicating all the necessary parameters involved in the study presented.

Based on the experimental work of Rao et al. [2], the dimensions are chosen for this geometry. Figure 8a shows the actual modeled geometry in OpenFOAM software. The working fluid is taken as FC-72, which has a saturation temperature of 306.3 K. The thermo-physical properties of FC-72 are specified in Table 1. The top part of the geometry is patched with vapor and the bottom part with liquid. The capillary inner diameter D is taken to be 2 mm and the total pipe length as 110 mm. The individual lengths of the evaporator and adiabatic sections are taken to be variable parameters. The initial pressure is maintained at 0.425 bar throughout the simulation model. The temperature of the evaporator is maintained at 55°C, which provides a 21.7° superheat. The reservoir pressure is kept at 0.42 bars. The length of the evaporator section is taken as 100 mm. The adiabatic section, located below the evaporator section, is of length 10 mm.

In all cases of simulations performed (to be discussed later this section), a certain initial time (0.015 sec) was given to the geometry depicted in Figure 8a, in order to stabilize itself and gain equilibrium. During this time, the liquid meniscus adjusts itself to equilibrate the forces in action,

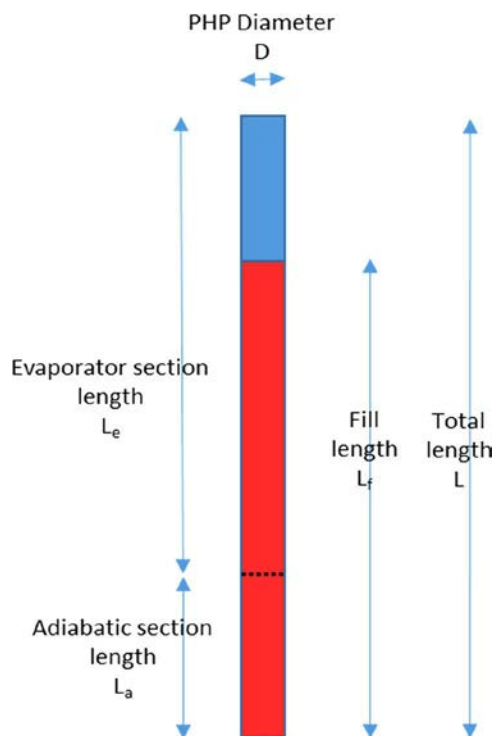


Figure 7. Schematic diagram of the part-unit cell of the PHP modeled in the present work.

resulting in the formation of a curved meniscus, as depicted in [Figure 8b](#). From this point onward, various case-specific conditions are provided to the equilibrium geometry for simulation. In the present work, contact angle is assumed to be static. There is no mention of any specific contact angle in the literature available for the case in consideration; hence, a static contact angle value of 50 is taken at the walls, keeping a limit on the gradient of the contact angle as zero.

Grid independence studies were performed on the model. The number of grid points used in the simulation for checking grid independence varied from a minimum of 3,750 to a maximum of 160,000. The maximum pressure developed in the vapor bubble is used as a criterion for deciding good independence. The results are plotted in [Figure 9](#). It can be seen from the plot that the maximum pressure developed in the bubble during OpenFOAM simulations agreed well with the experimental pressure result of Rao et al. [2] for a total grid point number of 40,000 and higher. The simulation value of maximum pressure also remained constant after a grid point number of 40,000. Hence the total number of grid points equal to 40,000 has been used for the simulations.

At the start of the simulation from the equilibrium state of the meniscus, the meniscus is located at the initial position in the evaporator section, determined by the liquid fill ratio. The downward motion of the meniscus commences as the liquid in the evaporator section starts evaporating.

Table 1. Thermophysical properties of FC-72 at 329.6 K and 1 atm.

Property	Liquid	Vapor
Kinematic viscosity (m^2/s)	2.797e-07	7.77e-07
Density (kg/m^3)	1,619.82	12.40
Thermal conductivity (W/mK)	5.216e-02	8.64e-03
Specific heat capacity (J/kgK)	1,098.41	885.04
Surface tension (N/m)	8.273e-03	
Enthalpy of vaporization (J/kg)	84,515	
Prandtl number	9.62	—

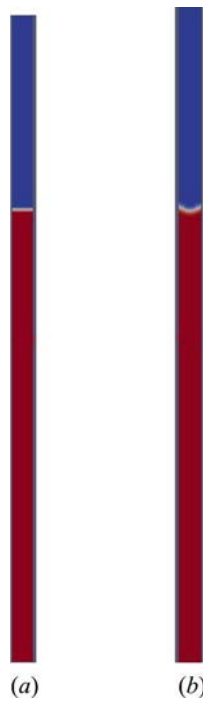


Figure 8. (a) The modeled geometry of the part-unit cell of the PHP in OpenFOAM; (b) equilibrium position for the part-unit cell of the PHP; the starting point for simulations.

Simulations show a rapid evaporation of the thin film, formed by the downward motion of the meniscus. The pressure in the vapor region increases due to the high rate of evaporation and resulting vapor-mass addition in the confined vapor space. Simultaneously, there is an expansion of the vapor space with the receding liquid meniscus. This causes a pressure reducing effect. However, the effect of vapor-mass addition leading to vapor pressure increase dominates over the expansion effect,

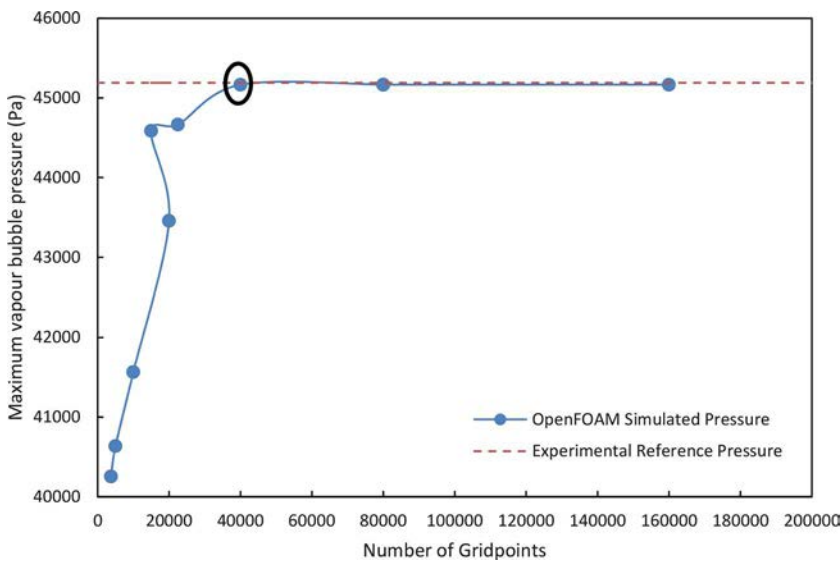


Figure 9. Grid independence study on the geometry; a comparison of the results with those of M. Rao et al. [2].

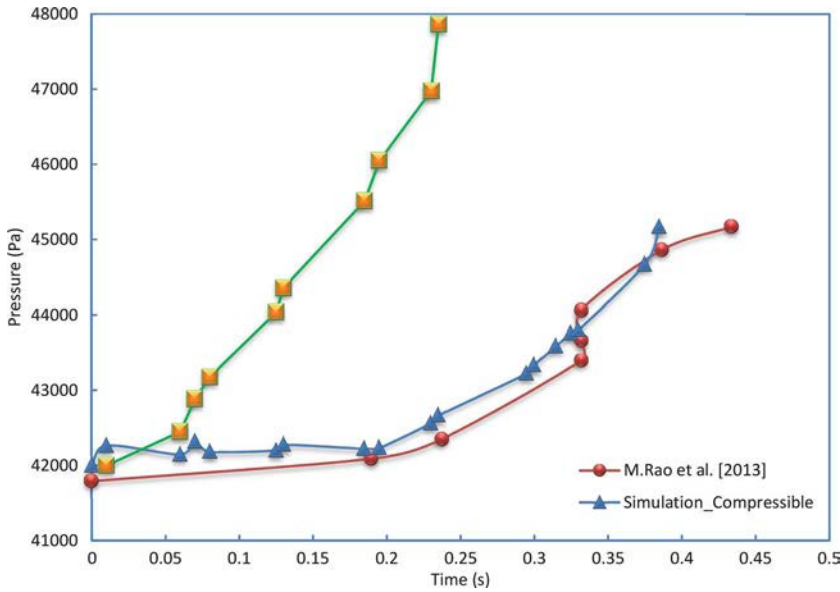


Figure 10. Comparison of vapor bubble pressure results of the OpenFOAM simulations with the experimental results of M. Rao et al. [2].

thereby resulting in a gradual vapor pressure increase with receding liquid meniscus. Hence, the maximum vapor pressure is observed when the liquid meniscus reaches the bottom end of the adiabatic section.

The results of compressible and incompressible solvers of the simulations have been plotted along with the experimental results of Rao et al. [2]. The agreement between the curves is shown in Figure 10. These plots correspond to the pressure variation within the vapor bubble in the evaporation and adiabatic sections. The OpenFOAM simulation results from the compressible solver are in good agreement with the experimental results of Rao et al. [2]. The total time taken by the simulated model of the compressible solver to reach the point of maximum pressure in the part-unit cell also agrees well with that of the experiments. This attests to the compressible solver being able to model the two effects described above – inertial and phase change. However, the incompressible solver predicts a very high maximum pressure value compared to the experimental and compressible solver results. Simultaneously, the time taken to reach the maximum pressure is also predicted to be very low (50% lower) compared with the experimental results. As discussed in the solver validation section, the incompressible solver fails to predict the inertial effects. In the present simulations, the incompressible solver could not predict the effect due to vapor bubble expansion, thus does not take into account the pressure decrease due to this process. As a result, the simulated pressure of the incompressible solver reaches a very high value. This results in a faster receding meniscus movement, and hence the time predicted by the incompressible solver for the meniscus to reach the bottom of the part-unit cell of PHP is very less.

4.2. Parametric study

In the geometry considered, the most important parameters affecting the performance of the PHP are the lengths of evaporator and adiabatic section, temperature of the evaporator, and the fluid fill ratio. A parametric study is performed on these three variables, evaluating their effect on the performance of the PHP. For the first variable, a nondimensional ratio of the length of the evaporator to the length of the adiabatic section (L_e/L_a) is considered. The difference between the evaporator temperature and the saturation temperature ($T_e - T_{sat}$) of the working fluid is considered as the second variable. The

Table 2. The lower and upper bounds for the variables in consideration.

Variable	Minimum value	Maximum value
L_e/L_a	2	10
T_e-T_{sat}	5	20
Fluid fill ratio	35	80

percentage of the PHP geometry, filled by the liquid, also called the liquid fill ratio, is considered as the third variable. The ranges of each of the variables described are presented in Table 2.

The performance of the PHP is exhibited in the total amount of heat it has transferred from the heat source to the heat sink. This can be accounted by considering both the maximum vapor bubble pressure and time for which the working fluid is in contact with PHP. The maximum vapor bubble pressure developed in the PHP is an indication of the rate of heat transfer in the PHP. The higher the maximum vapor bubble pressure reaches, the higher will be the heat transfer rate and, hence, the higher will be the total amount of heat transferred. The total time of contact of the working fluid with the part-unit cell (referred to as the working time subsequently) reflects the total amount of heat that is transferred from the evaporator to the working fluid.

4.2.1. Ratio of evaporator length to adiabatic section length (L_e/L_a)

The evaporator to adiabatic section length ratio is varied between 2 and 10 and its effect on the maximum pressure developed in the vapor bubble and working time of part-unit cell is simulated. Working time is considered as the time taken by the liquid meniscus in the simulation to reach the bottom end of the PHP part-unit cell. The evaporator temperature superheat and fluid fill ratio values are kept constant at 15°C and 70%, respectively. The results of these simulations are presented in Figure 11.

Figure 12 shows the time snapshots of volume fraction contours from the simulations in OpenFOAM. From the graphs presented in Figure 11, it can be observed that the maximum pressure in the vapor bubble decreases with increasing length of the evaporator. A similar trend is also reported for a full-scale PHP model experiment performed by Panyoyai et al. [20]. This was also the case with Fasula [21], wherein he observed that as the evaporator length increases, the heat flux decreased for all working fluids he experimented upon. From his study, he concluded that as the evaporator length decreases, the effective length between the condenser and the evaporator also

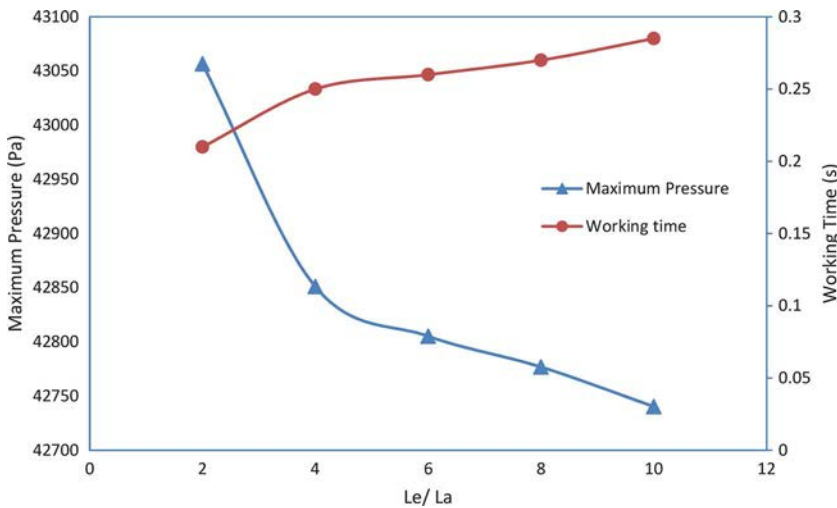


Figure 11. Effect of varying evaporator to adiabatic section length ratios on the maximum pressure and the working time of the part-unit cell of the PHP.

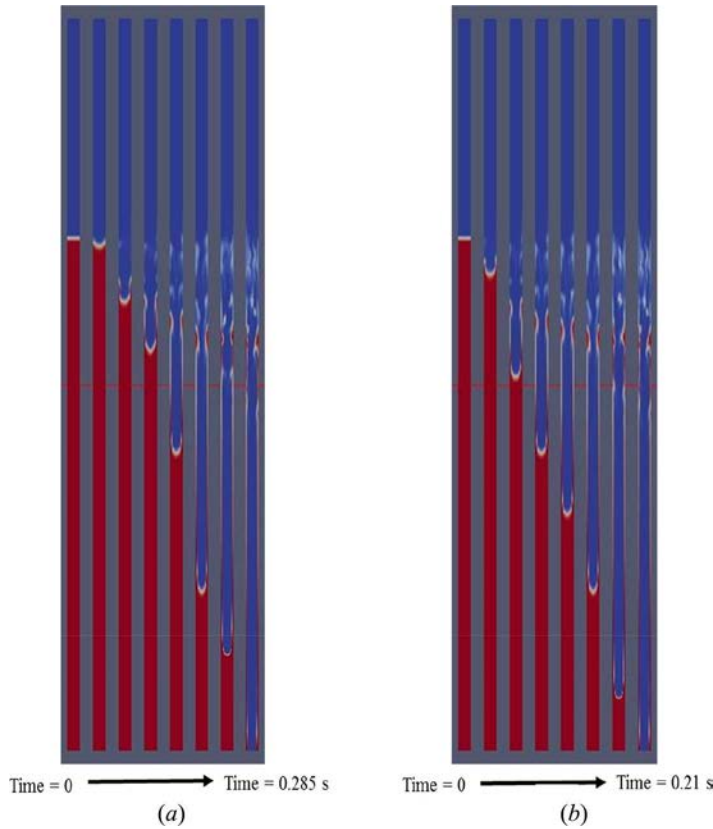


Figure 12. Time snapshots of volume fraction contours for the case of (a) $L_e/L_a = 10$; (b) $L_e/L_a = 2$.

decreases, allowing the heat to be effectively transferred by the working fluid. However, the present work resulted in the same trend for the variation of maximum pressure (heat flux in PHP) with evaporator length, even without the presence of any condenser. Hence, it can be concluded that the reason for this trend is more fundamental and lies within the working of the evaporator itself. There are two aspects to the change in vapor pressure. First, an addition of sensible heat due to evaporation results in increasing temperature of the vapor, thereby resulting in increased vapor pressures. Second, the bulk liquid evaporation results in vapor expansion, leading to pressure reduction in the vapor region. As the evaporator length increases, heat transfer and, hence, phase change happen from a larger bulk of the liquid. Hence, the amount of liquid compressing the vapor bubble at any time instant decreases. This effect outweighs the pressure-increasing effect of phase change and hence the vapor bubble pressure decreases with increase in evaporator length. For the case of working time of the part-unit cell of PHP, it increases almost linearly with increasing evaporator length, as can be observed from Figure 11. This is in accordance with the fact that as the maximum pressure inside the vapor bubble increases, keeping the fluid volume same, the working time of the part-unit cell of the PHP decreases.

4.2.2. Degree of evaporator superheat ($T_e - T_{sat}$)

The degree of evaporator superheat is varied between 5°C and 20°C. The evaporator to adiabatic section length ratio and fluid fill ratio values are kept constant at 10% and 70%, respectively. The results of these simulations are plotted in Figure 13.

Figure 14 shows the time snapshots of volume fraction contours from the simulations in OpenFOAM. From the graphs presented in Figure 13, it can be observed that the maximum pressure in the vapor bubble increases with increasing degree of superheat. As the superheat of the evaporator

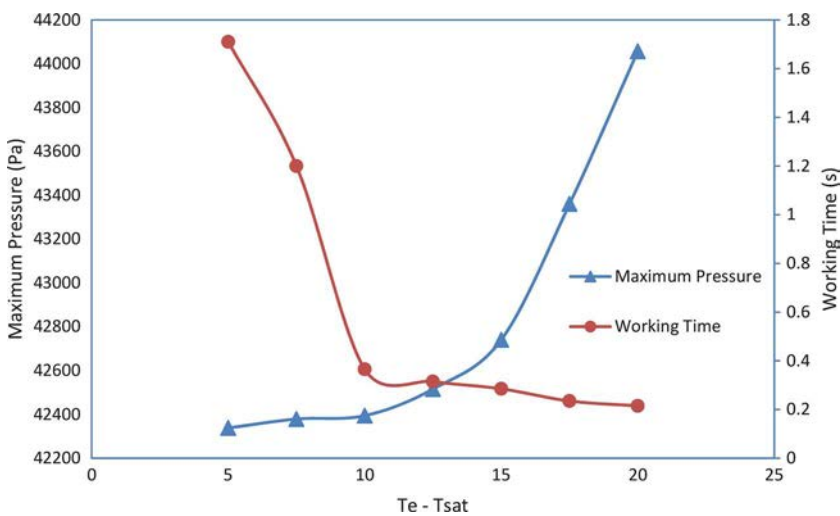


Figure 13. Effect of varying degrees of evaporator superheat on the maximum pressure and working time of the part-unit cell of the PHP.

increases, the heat transfer rate to the working fluid increases and hence the maximum pressure reached in the vapor bubble increases. For the case of working time of the part-unit cell of PHP, it decreases with increasing degree of superheat. Again, with an increase in maximum pressure attained by the vapor bubble, the working time of the part-unit cell decreases.

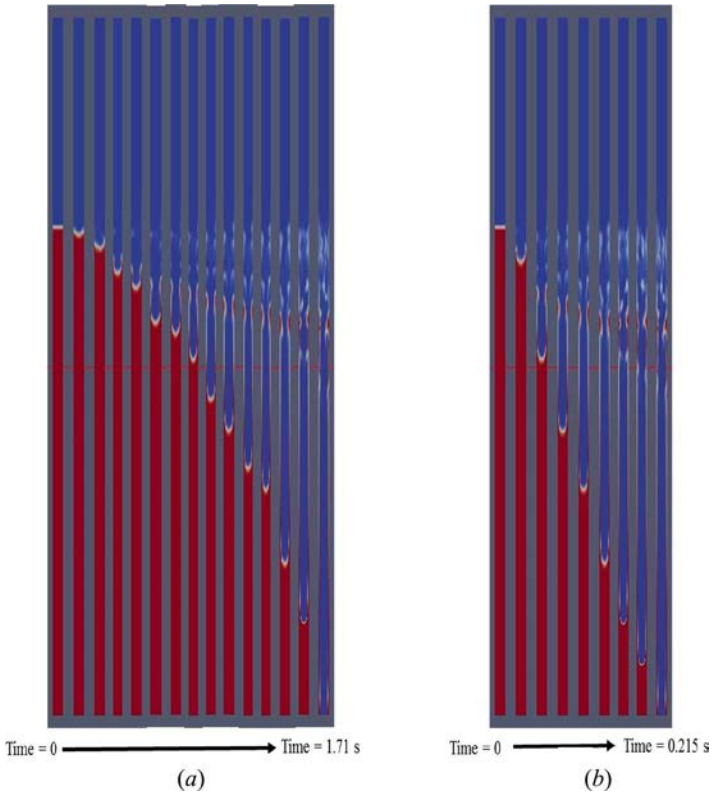


Figure 14. Time snapshots of volume fraction contours for the case of (a) $T_e - T_{sat} = 5$; (b) $T_e - T_{sat} = 20$.

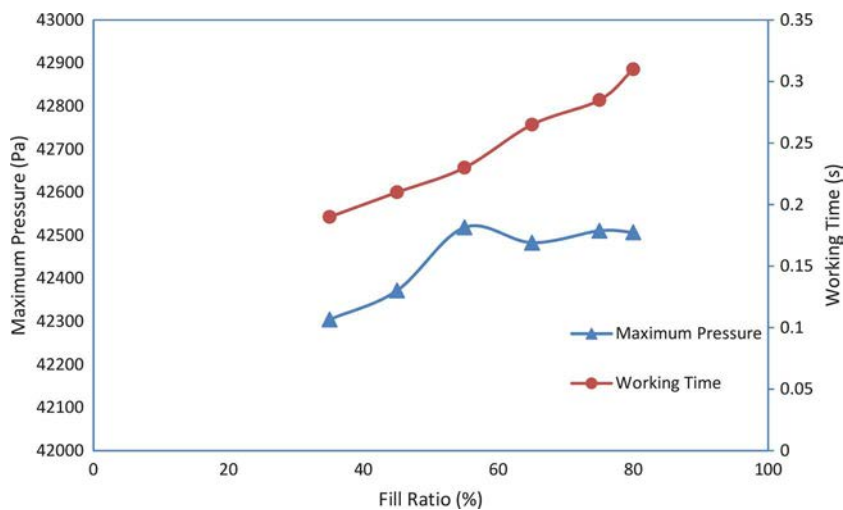


Figure 15. Effect of varying fluid fill ratios on the working time of the part-unit cell of the PHP.

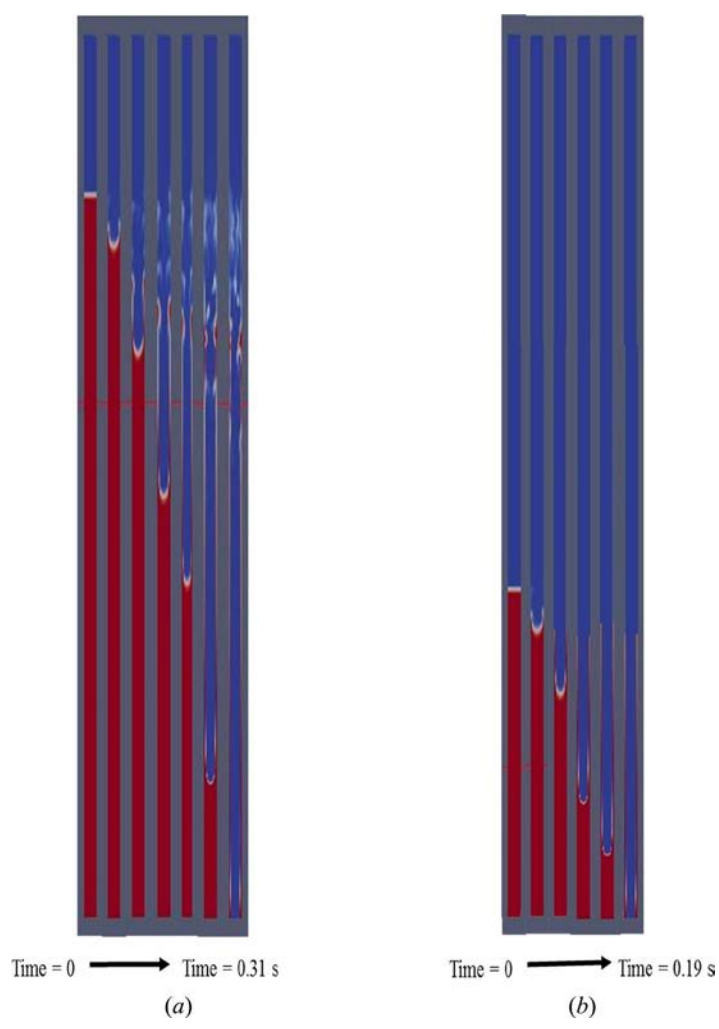


Figure 16. Time snapshots of the volume fraction contours for the case of (a) fill ratio = 80%; (b) fill ratio = 35%.

4.2.3. Fluid fill ratio

The fluid fill ratio is varied between 35% and 80%. The evaporator to adiabatic section length ratio and evaporator superheat values are kept constant at 10°C and 15°C, respectively. The results of these simulations are plotted in Figure 15.

Figure 16 shows the time snapshots of volume fraction contours from the simulations performed in OpenFOAM. From the graphs presented in Figure 15, it can be observed that the maximum pressure in the vapor bubble increases to a maximum value and then decreases steadily, with increasing fluid fill ratio. A similar trend has been found in various other studies, where the optimal fluid fill ratio was found to lie between 40% and 60%, for the maximum heat transfer from the PHP. This was also demonstrated by Khandekar and Groll [1]. At higher filling ratios (after 65% of liquid), the Taylor-Bubbles hindered the two-phase fluid motion, thus leading to lowering of the vapor pressure developed. For the case of working time of the part-unit cell of PHP, it increases almost linearly with increasing fluid fill ratio. This is due to the fact that although the pressure in the vapor bubble decreases after a certain fill ratio, the amount of working fluid increases with increasing fill ratio.

5. Conclusions

The work presented consists primarily of two parts – first the development, implementation, and validation of a compressible phase-change solver and second the numerical modeling of a part-unit cell of a PHP.

The compressible solver is implemented in OpenFOAM, which can be used to simulate phase change based on the VOF method. This present work involves the implementation of an interface reconstruction algorithm, developed by Kunkelmann [16] and the contact-line evaporation model of Stephen and Busse [15]. Owing to the lack of a single benchmark result for compressible phase-change problems, the validation of the solver was carried out in three stages.

1. Unconstrained adiabatic bubble expansion and contraction.
2. Unconstrained isothermal phase change.
3. Constrained Taylor-Bubble development.

The first and the second cases are numerically validated using approximations and modifications of the RP equation, whereas the third case is used to test the working of the compressible phase-change solver in the formation and development of a TB. With the validated model, a part-unit cell of a PHP containing only the evaporator and the adiabatic sections is modeled. This model is used to validate the experimental results of Rao et al. [2]. A parametric study is performed, taking the length ratio of evaporator to adiabatic section, degree of superheat of the evaporator section, and liquid fill ratio as the variables. With an increasing length ratio of evaporator to adiabatic section from 2 to 8, the maximum vapor pressure decreased while the working time of the part-unit cell of the PHP increased. The maximum vapor pressure is observed to increase and working time decrease with an increasing value of evaporator superheat from 5° to 20°. An optimum filling ratio exists (around 50%) where the maximum vapor pressure reaches the maximum. Working time is observed to decrease with increasing fill ratio (35%–80%).

In summary, simulations confirmed that the compressible phase-change solver is essential in gaining a fundamental understanding and developing a compressible phase-change model, describing the working of a PHP.

Acknowledgments

The authors would like to acknowledge the technical support provided by Prof. Dr.-Ing. Peter Stephan and Dr.-Ing. Stefan Batzdorf of Technische Universität Darmstadt toward successful completion of the present work.

References

- [1] S. Khandekar, N. Dollinger, and M. Groll, Understanding Operational Regimes of Closed Loop Pulsating Heat Pipes: An Experimental Study, *Appl. Therm. Eng.*, vol. 23, no. 6, pp. 707–719, 2003.
- [2] M. Rao, et al. Understanding Transport Mechanism of a Self-Sustained Thermally Driven Oscillating Two-Phase System in a Capillary Tube, *Int. J. Heat Mass Transfer*, vol. 65, pp. 451–459, 2013.
- [3] Z. J. Zuo, M. T. North, and K. L. Wert, High Heat Flux Heat Pipe Mechanism for Cooling of Electronics, *Compon. Packag. Technol. IEEE Trans.*, vol. 24, no. 2, pp. 220–225, 2001.
- [4] T. N. Wong, et al. Theoretical Modeling of Pulsating Heat Pipe. Proceedings of the 11th International Heat Pipe Conference, Tokyo, Japan, 1999.
- [5] M. B. Shafii, A. Faghri, and Y. Zhang, Thermal Modelling of Unlooped and Looped Pulsating Heat Pipes, *J. Heat Transfer*, vol. 123, no. 6, pp. 1159–1172, 2001.
- [6] H. B. Ma, et al. An Experimental Investigation of Heat Transport Capability in a Nanofluid Oscillating Heat Pipe, *J. Heat Transfer*, vol. 128, no. 11, pp. 1213–1216, 2006.
- [7] Y. Zhang and A. Faghri, Heat Transfer in a Pulsating Heat Pipe with Open End, *Int. J. Heat Mass Transfer*, vol. 45, no. 4, pp. 755–764, 2002.
- [8] A. Mukherjee and S. G. Kandlikar, Numerical Simulation of Growth of a Vapour Bubble during Flow Boiling of Water in a Microchannel, *Microfluid. Nanofluid.*, vol. 1, no. 2, pp. 137–145, 2005.
- [9] A. Mukherjee, Contribution of Thin-Film Evaporation during Flow Boiling Inside Microchannels, *Int. J. Therm. Sci.*, vol. 48, no. 11, pp. 2025–2035, 2009.
- [10] J. R. Thome, V. Dupont, and A. M. Jacobi, Heat Transfer Model for Evaporation in Microchannels. Part I: Presentation of the Model, *Int. J. Heat Mass Transfer*, vol. 47, no. 14, pp. 3375–3385, 2004.
- [11] X. Liu, and Y. Hao, Numerical Simulation of Vapour-Liquid Two-Phase Flow in a Closed Loop Oscillating Heat Pipe, ASME 2009 International Mechanical Engineering Congress and Exposition. American Society of Mechanical Engineers, 2009.
- [12] A. Pattamatta, M. Freystein, and P. Stephan, A Parametric Study on Phase Change Heat Transfer Due to Taylor-Bubble Coalescence in a Square Minichannel, *Int. J. Heat Mass Transfer*, vol. 76, pp. 16–32, 2014.
- [13] S. Hardt and F. Wondra, Evaporation Model for Interfacial Flows Based on a Continuum-Field Representation of the Source Terms, *J. Comput. Phys.*, vol. 227, no. 11, pp. 5871–5895, 2008.
- [14] C. W. Hirt and B. D. Nichols, Volume of Fluid (VOF) Method for the Dynamics of Free Boundaries, *J. Comput. Phys.*, vol. 39, no. 1, pp. 201–225, 1981.
- [15] J. U. Brackbill, D. B. Kothe, and C. I. Zemach, A Continuum Method for Modelling Surface Tension, *J. Comput. Phys.*, vol. 100, no. 2, pp. 335–354, 1992.
- [16] C. Kunkelmann, and P. Stephan, CFD Simulation of Boiling Flows Using the Volume-of-Fluid Method within OpenFOAM, *Numerical Heat Transfer, Part A*, vol. 56, no. 8, pp. 631–646, 2009.
- [17] P. C. Stephan and C. A. Busse, Analysis of the Heat Transfer Coefficient of Grooved Heat Pipe Evaporator Walls, *Int. J. Heat Mass Transfer*, vol. 35, no. 2, pp. 383–391, 1992.
- [18] V. P. Carey, Liquid-Vapor Phase-Change Phenomena, Hemisphere Publishing Corporation, Carlsbad, US, 1992.
- [19] M. S. Plesset and S. A. Zwick, The Growth of Vapour Bubbles in Superheated Liquids, *J. Appl. Phys.*, vol. 25, no. 4, pp. 493–500, 1954.
- [20] N. Panyoyai, P. Terdtoon, and P. Sakulchangsatjatai, Effects of Aspect Ratios and Number of Meandering Turns on Performance Limit of an Inclined Closed-Loop Oscillating Heat Pipe, *Energy Res. J.*, vol. 1, no. 2, p. 91, 2010.
- [21] C. Fasula, Oscillating Heat Pipes (OHP). Masters of Science in Mechanical Engineering and Applied Mechanics, University of Rhode Island, Kingston, US, 2009.